The Journal of Immunology

Flow Cytometry Data Preparation Guidelines for Improved Automated Phenotypic Analysis

Daniel Jimenez-Carretero, José M. Ligos, María Martínez-López, David Sancho and María C. Montoya

J Immunol 2018; 200:3319-3331; ;
doi: 10.4049/jimmunol.1800446
http://www.jimmunol.org/content/200/10/3319

This information is current as of November 16, 2022.

Supplementary Material **http://www.jimmunol.org/content/suppl/2018/05/01/200.10.3319.DCSupplemental**

References This article **cites 36 articles**, 5 of which you can access for free at:
http://www.jimmunol.org/content/200/10/3319.full#ref-list-1

Why *The JI*? Submit online.

- **Rapid Reviews! 30 days*** from submission to initial decision
- **No Triage!** Every submission reviewed by practicing scientists
- **Fast Publication!** 4 weeks from acceptance to publication

**average*

Subscription Information about subscribing to *The Journal of Immunology* is online at:
http://jimmunol.org/subscription

Permissions Submit copyright permission requests at:
http://www.aai.org/About/Publications/JI/copyright.html

Email Alerts Receive free email-alerts when new articles cite this article. Sign up at:
http://jimmunol.org/alerts

The Journal of Immunology is published twice each month by
The American Association of Immunologists, Inc.,
1451 Rockville Pike, Suite 650, Rockville, MD 20852
Copyright © 2018 by The American Association of Immunologists, Inc. All rights reserved.
Print ISSN: 0022-1767 Online ISSN: 1550-6606.

Downloaded from http://www.jimmunol.org/ at Fundacion (CNIC) on November 16, 2022

Immunology Notes and Resources

The Journal of Immunology

Flow Cytometry Data Preparation Guidelines for Improved Automated Phenotypic Analysis

Daniel Jimenez-Carretero,* José M. Ligos,* María Martínez-López,† David Sancho,† and María C. Montoya*

Advances in flow cytometry (FCM) increasingly demand adoption of computational analysis tools to tackle the ever-growing data dimensionality. In this study, we tested different data input modes to evaluate how cytometry acquisition configuration and data compensation procedures affect the performance of unsupervised phenotyping tools. An analysis workflow was set up and tested for the detection of changes in reference bead subsets and in a rare subpopulation of murine lymph node CD103$^+$ dendritic cells acquired by conventional or spectral cytometry. Raw spectral data or pseudospectral data acquired with the full set of available detectors by conventional cytometry consistently outperformed datasets acquired and compensated according to FCM standards. Our results thus challenge the paradigm of one-fluorochrome/one-parameter acquisition in FCM for unsupervised cluster-based analysis. Instead, we propose to configure instrument acquisition to use all available fluorescence detectors and to avoid integration and compensation procedures, thereby using raw spectral or pseudospectral data for improved automated phenotypic analysis. ***The Journal of Immunology*****, 2018, 200: 3319–3331.**

Flow cytometry (FCM) is the most widely used single-cell analysis technique because of its ability to measure multiple parameters, which allows the phenotypic and functional study of cell populations. FCM has undergone a technological revolution in recent years, affecting both instrumentation and reagent availability, greatly increasing the number of parameters that can be analyzed simultaneously in a single cell (1, 2). The most widely available cytometry technology is fluorescence-based conventional FCM; however, it suffers from limitations in its multiparametric capability because of fluorochrome spectral overlap (3–5). Technological developments in conventional FCM instrumentation have focused on increasing the number of detectors, reaching as many as 30 in some instruments. Spectral FCM technology allows the acquisition of a continuous range of wavelengths for each individual cell regardless of the fluorochrome spectrum emission (6–8). Spectral FCM thus enables multicolor analysis through its ability to distinguish fluorochromes with overlapping spectra; moreover, the optical configuration and deconvolution algorithms available for processing spectral FCM data provide higher resolution. This technological evolution of FCM, together with the recent appearance of mass cytometry, which enables the quantification of over 40 parameters in individual cells, presents major analytical challenges due to the increased data dimensionality. This has prompted the development of computational tools that allow semiautomatic analysis and interpretation of high-dimensional data. These tools are widely used in the mass cytometry field and are progressively being adopted by the FCM community (1, 9, 10). However, widespread use of these computational tools has been hampered by the historically low-dimensional nature of conventional FCM data and the lack of procedures for automated data handling in the fluorescence-based FCM field, in which bench scientists and analysts are still accustomed to manual-gating approaches. Gating is a critical bottleneck in

*Unidad de Celómica, Área de Biología Celular y del Desarrollo, Centro Nacional de Investigaciones Cardiovasculares Carlos III, Madrid E28029, Spain; and †Laboratorio de Inmunobiología, Área de Fisiopatología del Miocardio, Centro Nacional de Investigaciones Cardiovasculares Carlos III, Madrid E28029, Spain

ORCID: 0000-0001-8878-7028 (M.C.M.).

Received for publication March 23, 2018. Accepted for publication March 23, 2018.

This work was supported by Grants BIO2014-62200-EXP and PI-FIS-2016 from the Spanish Ministry of Economy, Industry, and Competitiveness (MEIC) (to M.C.M.) and a University Teaching Training Program fellowship (AP2010-5935) from the Spanish Ministry of Education (to M.M.-L.). Work in the D.S. laboratory is funded by the Centro Nacional de Investigaciones Cardiovasculares (CNIC) and grants from MEIC, Agencia Estatal de Investigación, the European Regional Development Fund (SAF2016-79040R), the European Commission (635122-PROCROP H2020), the European Research Council (ERC-2016-Consolidator Grant 725091), and the Acteria Foundation. CNIC is supported by MEIC and the Pro-CNIC Foundation and is a Severo Ochoa Center of Excellence (SEV-2015-0505).

D.J.-C. contributed to the design of the study, performed experimental work, data analysis, interpretation of results, and preparation of figures, and contributed to manuscript writing; J.M.L. conceived the initial study, performed experimental work, data analysis, interpretation of results, and preparation of figures, and contributed to manuscript writing; M.M.-L. contributed to the design of the dendritic cell study, performed skin-draining lymph node preparation, contributed to interpretation of results, and did critical reading of the manuscript; D.S. contributed to the design of the dendritic cell study and did critical reading of the manuscript; and M.C.M. supervised the project and wrote the manuscript.

Address correspondence and reprint requests to Dr. José M. Ligos and Dr. María C. Montoya, Centro Nacional de Investigaciones Cardiovasculares Carlos III, Calle de Melchor Fernández Almagro 3, Madrid E28029, Spain. E-mail addresses: jmligos@cnic.es (J.M.L.) and mmontoya@cnic.es (M.C.M.)

The online version of this article contains supplemental material.

Abbreviations used in this article: AP, automated phenotyping; DC, dendritic cell; FCM, flow cytometry; fcs, flow cytometry standard; KO, knockout; LN, lymph node; MHC II, MHC class II; t-SNE, t-Distributed Stochastic Neighbor Embedding; WT, wild type.

Copyright © 2018 by The American Association of Immunologists, Inc. 0022-1767/18/$35.00

www.jimmunol.org/cgi/doi/10.4049/jimmunol.1800446

Downloaded from http://www.jimmunol.org/ at Fundacion (CNIC) on November 16, 2022

high-dimensional FCM data analysis because it is labor intensive and subject to individual user bias (2). In addition, gating requires prior knowledge of the populations of interest, thus hindering the discovery of previously undefined yet meaningful cell populations. The automated phenotyping (AP) of cell populations using unsupervised clustering techniques has therefore opened a promising avenue for the FCM field to reach its full potential and avoid user-derived analytical hurdles.

The aim of this study was to provide scientists with guidelines for the preparation of data for AP that can be adapted to whatever FCM technology is available in their laboratories. The intention was not to compare the performance of different FCM technologies or clustering algorithms. We established a reference standard experiment and prepared datasets using conventional and spectral FCM. The datasets contain both raw data and data subjected to different spillover correction methods. We also implemented an automated analysis framework for the detection of changes in subpopulations among multiple samples using state-of-the-art unsupervised algorithms. To our knowledge, this is the first systematic evaluation to demonstrate the convenience of avoiding standard configurations for FCM acquisition in attempts to improve automated phenotypic analysis. Based on our findings, we recommend cytometrists to take advantage of the full detector configuration available in the instrument at hand instead of restricting themselves to the conventional detection channels matching the fluorescence emission of the fluorophores in use. Moreover, this study reveals the advantages of using raw data over compensated or integrated data to ensure the highest accuracy in automated phenotypic analysis.

Materials and Methods

Mice

Mice were bred in specific pathogen-free conditions. Batf3$^{-/-}$ mice back crossed more than 10 times to the C57BL/6 background were kindly provided by Dr. K.M. Murphy (Washington University, St. Louis, MO) (11). These mice were further back crossed with C57BL/6 mice to establish wild type (WT) and Batf3$^{-/-}$ mouse colonies from the heterozygotes. Animal studies were approved by the local ethics committee. All animal procedures conformed to EU Directive 2010/63EU and Recommendation 2007/526/EC regarding the protection of animals used for experimental and other scientific purposes, enforced in Spanish law under Real Decreto 1201/2005.

Skin-draining lymph node preparation

Single-cell suspensions of skin-draining lymph nodes (LNs) (inguinal, axillary, brachial, and auricular) were prepared by digestion with Liberase TL Research Grade and DNAse I from bovine pancreas (Both from Sigma-Aldrich) as previously described (12).

Flow cytometry

All stainings were performed in 0.5% BSA in PBS for 30 min on ice. UltraComp eBeads Compensation Beads (Life Technologies, Carlsbad, CA) were stained with the following anti-mouse Abs (BD Biosciences, San Jose, CA): anti–CD45-V450, anti–CD45R-AF647, anti–CD4-PE, and/or anti–CD4-BV711. Single-cell suspensions from LNs were blocked with FC Block (BD Biosciences) and stained with Abs (BD Biosciences or BioLegend, San Diego, CA) to detect MHC class II (MHC II)-FITC (2G9), CD40-PE (3/23), CD3-PE-CF594 (145-2C11), Ly6c-PerCP-CY5.5 (HK/4), CD11b-PE-CY7 (MI/70), CD103-BV421 (M290), CD45-BV570 (30-F11), CD19-BV605 (1D3), CD4-BV711 (GK1.5), CD11c-APC (HL3), and CD8-APC-Fire750 (S3-G.7). After staining, beads or cells were washed with PBS containing 0.5% BSA. Conventional FCM data were obtained in a BD LSRFortessa (BD Biosciences) cytometer equipped with four lasers and 18 detectors (16 for fluorescence and two scatters). This system was configured as follows: seven detectors for the 405 nm laser, four detectors for the 488 nm laser (two of them for scatter), four detectors for the 561 nm laser, and three detectors for the 640 nm laser. Photomultiplier tube amplification was adjusted to keep the autofluorescence signal 2.5 SD over the electronic noise while keeping the signal within the detector's linearity range. Spectral FCM data were obtained using an SP6800 Spectral Cell Analyzer (Sony Biotechnology, San Jose, CA) flow cytometer equipped with three lasers and 68 detectors (66 for fluorescence and two for scatter). This system was configured as follows: 34 detectors for the 488 nm laser (32 for continuous fluorescence between 400 and 800 nm and two for scatter) and 34 detectors for the collinear 405 and 638 nm lasers. Photomultiplier tube amplification was set to keep all signals within the detector's linearity scale.

FCM data processing

Data from the conventional flow cytometer were analyzed using FlowJo (FlowJo, Ashland, OR) and FCS Express (De Novo Software, Glendale, CA). In all cases, compensated data were obtained from single-stained UltraComp eBeads using the automatic software tool without further adjustment. Data from the spectral flow cytometer were analyzed with SP6800 software (Sony Biotechnology). Raw spectral data in comma-separated value format were obtained using a Raw File Converter kindly provided by Sony Biotechnology. Uncompensated, spectral unmixed, and conventionally compensated datasets were stored in files according to the flow cytometry standard (fcs) 3.0 format with SP6800 software. For unmixed and conventionally compensated data, single-stained UltraComp eBeads were used as compensation controls for the automatic tool without further adjustment.

Preparation and cleaning of FCM samples

Multi-input fcs files were generated by merging the different data input modes exported with the proprietary software of the specific cytometry equipment used in each case. For each sample, the three fcs files from conventional flow cytometer acquisition containing uncompensated, compensated, and pseudospectral (uncompensated from all fluorescence detectors available) channels were concatenated as new parameters by directly matching events to form a single fcs file with all the channels from the three conventional input modes. Similarly, for each sample, the comma-separated value file containing raw spectral data and the three fcs files from spectral cytometer acquisition containing uncompensated, conventionally compensated, and spectrally unmixed area channels were concatenated in a single multi-input fcs file. We disregarded channels corresponding to detectors 20–23 in the raw spectrum because they are bound or affected by the active Notch filter. Data were cleaned in these multi-input fcs files by gating single events and removing outliers for all the channels, thereby ensuring maintenance of the same events for all corresponding data input modes during subsequent processing steps. Additionally, for the cell-based analysis, debris was excluded and CD45+ cells were gated.

Automatic analysis workflow

The proposed automated pipeline for studying population changes among multiple FCM samples (Fig. 1D) comprises six stages: 1) preprocessing of FCM data to transform fluorescence signals into a linear scale, 2) subsampling of FCM events to facilitate suitable processing of full datasets and multiple samples, 3) dimensionality reduction of high-dimensional fluorescence signals for visualization purposes, 4) automatic clustering for unbiased detection of subpopulations, 5) upsampling of FCM events to extend results to the whole set of original events and files export, and 6) sample comparison and population identification.

Preprocessing of FCM data. Samples (fcs files) were transformed separately using an automated Logicle function with a unique parameter set estimated automatically (13) for all channels involved in the analysis of a specific data input mode. This biexponential transformation provides an effective and robust way to correctly linearize fluorescence signals independently both of the scale of the data (which may differ depending on the cytometer or data input mode) and of the presence or absence of information in each channel (especially important in supplemental channels included in pseudo- and full-spectral data).

Subsampling of FCM events. A subsampling procedure was applied to each sample to reduce the number of events bound for the posterior clustering and dimensionality-reduction steps. This was done to overcome the computational limitations (time, memory, and resources) of jointly processing large and multiple samples for comparative analyses. Local-density–dependent downsampling (14) was performed for each individual sample separately to equalize the density of events, achieving more similar representation of both rare and abundant populations and preventing rare types from vanishing during subsampling (Supplemental Fig. 1). The pseudo-aleatory component of the method encourages a different subsampling output with every run. In all experiments, data were downsampled to 2500 events per sample by using default parameters for the algorithm and all channels involved in the specific data input mode. *k*-Nearest neighbors was later used to assign each original

Downloaded from http://www.jimmunol.org/ at Fundacion (CNIC) on November 16, 2022

event to its closest downsampled event. Fluorescence fingerprinting of subsampled events was constructed by averaging the fluorescence signals from the corresponding original events.

Dimensionality reduction. To visualize population representations and clustering results, we used the Barnes-Hut t-Distributed Stochastic Neighbor Embedding (t-SNE) (15) implementation in R (https://github.com/jkrijthe/Rtsne) with the recommended parameters (perplexity = 30, θ = 0.5, iterations = 1000, Euclidean distance). Because the t-SNE method is completely data dependent and provides no explicit function for projections, different runs and different samples report different outputs. For this reason, events from all downsamples were processed together, providing a common t-SNE map distribution allowing sample comparison.

Automatic clustering. All subsampled events from the whole sample set were used jointly for unbiased clustering, providing a common detection of subpopulations that allowed sample comparison. We tested automatic clustering algorithms recommended by Weber and Robinson (16) that allowed runs in script mode and required no prior information about the size or number of expected clusters. We also tested algorithms relying on t-SNE projections. All algorithms tested, including PhenoGraph (17), DenseVM (18), ClusterX (19), and flowMeans (20), were run in R with the default settings. PhenoGraph was selected as the default clustering method in the automatic analysis workflow for further experiments because it reported the best lower 99% confident interval of F1 scores (see *Materials and Methods*, Evaluation of clustering results) when analyzing conventional FCM data input in the traditional way (CONV_4ch_CC) using the reference dataset (Supplemental Fig. 2).

Upsampling of FCM events. By using the correspondence between original events and closest downsampled events, computed in step two, we could infer t-SNE coordinates and cluster membership for the whole set of original events from a specific sample from the results obtained in the previous two stages by direct assignment. A noisy version of t-SNE coordinates was also computed to improve the visualization of t-SNE maps in terms of point density by calculating a weighted mean of coordinates from a selection of subsampled events. For each original event, we first selected the five most similar subsampled events in terms of fluorescence fingerprinting and kept only the three of them with the closest t-SNE map location with respect to the initial inferred t-SNE coordinates. Their coordinates were then weighted by their proximity and averaged to obtain the final noisy t-SNE location. Results of cluster membership and t-SNE coordinates were included as new parameters for each original sample and saved as fcs files.

Sample comparison and population identification. Once analyzed, fcs files were processed to generate diverse outputs for data visualization and comparative analyses. To identify populations, the workflow displays t-SNE maps for individual samples or sample sets colored according to cluster number or to the intensity of expression of the different fluorescence markers. In addition, heatmap representations of fluorescence fingerprints of clusters can be displayed. To compare samples, heatmaps are provided displaying frequencies of events in each sample and the fold-change with respect to controls,

$$fc(x) = sign(|x| - |ctrl|) \cdot \left(\frac{max(|x|,|ctrl|)}{min(|x|,|ctrl|)} - 1 \right), \; where |A| = frequency(A),$$

together with statistics reporting significance.

Software resources

The automated analysis pipeline was implemented as a script in MATLAB (R2017a, Parallel Computing and Statistics Toolbox) and R (version 3.3.2, packages flowCore, cytofkit, flowMeans) for stages one through five. Graphical representations for stage six were obtained with MATLAB. t-SNE maps colored by different parameters were represented using the MATLAB-based *cyt* tool (21).

Evaluation of clustering results

The F1 measure (harmonic mean of precision and recall) was used to score the correspondence between classes or reference standard populations (manually gated) and automated clustering outputs. Precision, recall, and F1 scores varies varied between 0 and 1, with high values signifying a low proportion of false-positives in precision and a low proportion of false-negatives in recall. An F1 score of 1 indicates a perfect reproduction of reference classes with the specific clustering results. The Hungarian assignment algorithm (22) was used to solve the problem of mapping one–to–one clusters and reference populations by maximizing the sum of F1 scores across all reference classes. This solution provides a fairer evaluation strategy compared with the individual maximization of F1 scores for each reference population or output cluster (16) by not mapping a single cluster to more than one reference population and including the possibility of clusters not matching any reference class. The reported F1 values in the text correspond to final scores obtained for all events and reference classes from all samples in a specific analysis (one F1 score per run).

Statistics

Different data inputs from conventional and spectral acquisition modes were processed independently (10 times each). Statistical analyses were performed in Prism v5.0 using two-sided tests. Clustering performances were compared across different data input modes in reference bead datasets (Fig. 4A) and cell-based datasets (Fig. 5B) by repeated measures one-way ANOVA and Tukey's multiple comparison test (adjusted p values: $^{*}p < 0.05$, $^{**}p < 0.01$, $^{***}p < 0.001$). Significant cluster frequency differences ($^{*}p < 0.01$) between WT and knockout (KO) sample sets (Fig. 6D, 6F) were detected by t tests.

Figures showing representative results

All examples showing t-SNE maps and specific clustering results (Figs. 2, 4C, 4D, 5, 6C–J, Supplemental Figs. 3, 4) correspond to outputs obtained with the run that achieved the F1 score closest to the median value from all 10 independent runs of a specific data input mode.

Availability

Reference bead and cell-based datasets are freely available through FlowRepository (http://flowrepository.org/) via the following experiment IDs: FR-FCM-ZYGA (MIX beads) and FR-FCM-ZYHL (murine skin-draining LNs). Code for running the AP workflow can be accessed via GitHub: https://github.com/nielintos/AP-workflow.

Results

Establishment of a reference standard experiment and an AP framework for FCM data analysis

Most experimental FCM approaches involve the analysis of cell populations with differing phenotypic signatures in a series of samples. To simulate this experimental approach as a benchmark for evaluation purposes, we prepared a synthetic FCM dataset (Fig. 1A, 1B). Test tubes were prepared containing capture beads stained with single, double, triple, and quadruple combinations of Abs directly conjugated to V450, PE, AF647, and BV711 fluorochromes (Fig. 1A). The fluorescent signals were individually acquired by conventional FCM and compensated for spillover correction to obtain fcs files, as detailed in the *Materials and Methods*. For reference purposes, each file was independently analyzed by manual gating to ascribe a reference class to each subset of beads labeled with a specific fluorochrome or fluorochrome combination (RefClass no. 1 to no. 14). The manual gating strategy used is shown for two examples: the test tubes for V450 single staining and AF647/BV711 double staining (Fig. 1B). Finally, all labeled events (beads) from the different test tubes were concatenated in a new joint synthetic file (named "CONV_MIX1"). This file is considered a synthetic sample because it contains all labeled subsets corresponding to the real reference classes included in the different test tubes in the whole experiment. The most common analytical goal in FCM experiments is to detect changes in the frequencies of populations among a series of samples. This is especially challenging with rare populations. To simulate this experimental scenario, the CONV_MIX1 file was modified by randomly reducing the number of events for a specific subset of beads by half (RefClass no. 6, AF647/BV711 stained beads). This reduction was done in six serial steps, yielding six new synthetic files (CONV_MIX2-MIX7), each with a different proportion of the RefClass no. 6 population. These were treated as synthetic samples in subsequent analysis. In the original CONV_MIX1 file, the RefClass no. 6 bead subset represented 7.16% of the full dataset; this proportion was reduced to 3.71, 1.89, 0.95, 0.48, and 0.24% in files CONV_MIX2 through CONV _MIX6. In file CONV_MIX7, the RefClass

Downloaded from http://www.jimmunol.org/ at Fundacion (CNIC) on November 16, 2022

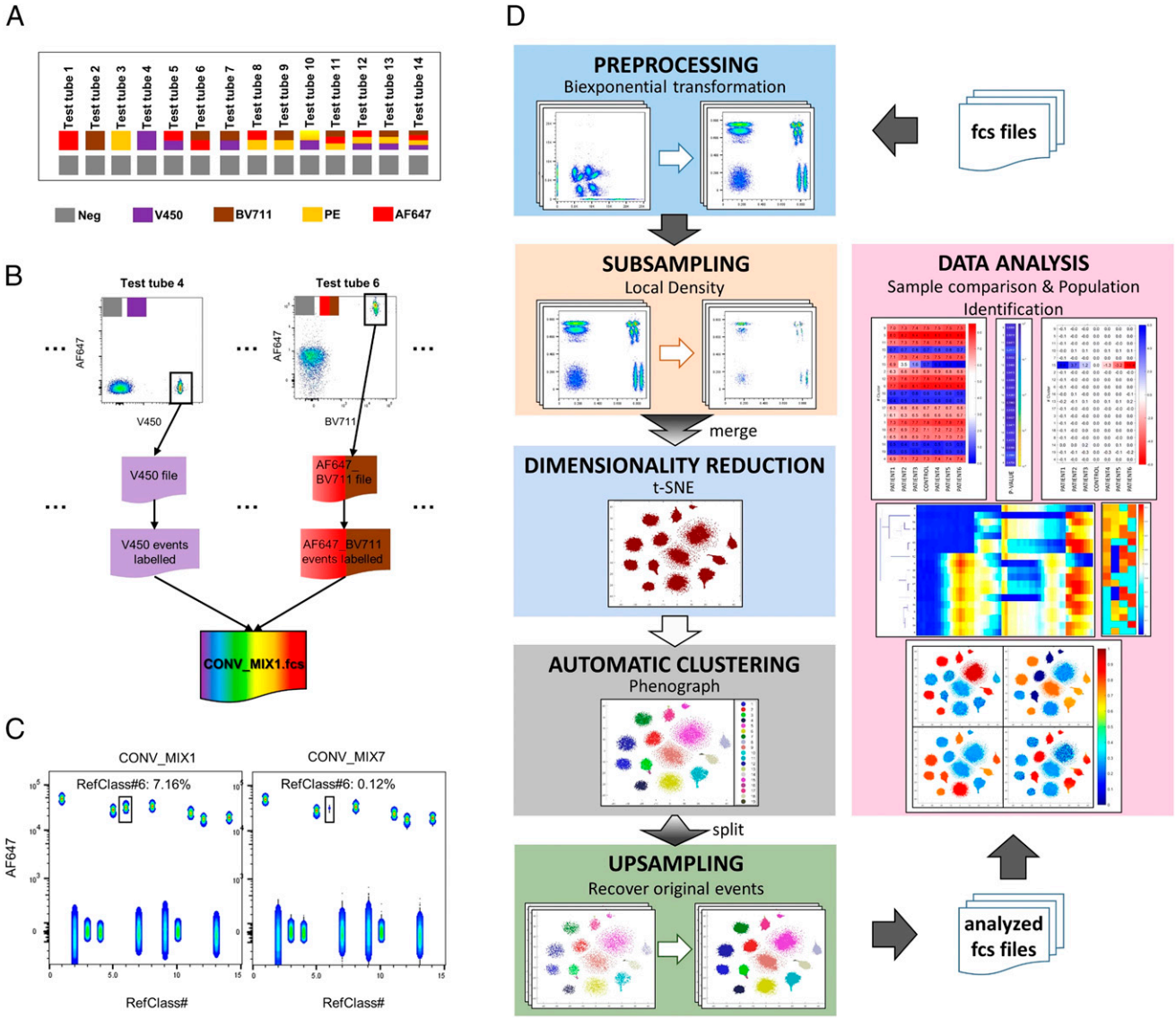

FIGURE 1. Schematic representation of reference standard experiment and automated analysis framework. (**A**) Test tubes contain different bead combinations, including unstained beads (Neg) and beads stained with varying combinations of the fluorochromes V450, PE, AF647, and BV711. (**B**) Reference class labeling procedure and synthetic file (sample) preparation. The panels represent test tube 4, containing V450 single-stained beads, and test tube 6, containing AF647/BV711 double-stained beads. Signals were acquired in a conventional flow cytometer, and stained beads were manually gated, exported as single file, and labeled as RefClass no. 4 and no. 6, respectively. The synthetic file (CONV_MIX1.fcs) is obtained by merging files acquired from all test tubes, each containing stained events labeled as Ref Classes. (**C**) The original file (CONV_MIX1.fcs) and the file obtained by reducing the number of RefClass no. 6 events by half (CONV_MIX7.fcs) after six iterations. All events are plotted according to RefClass labels. Events labeled as RefClass no. 6 are highlighted with a square, and the percentage of the total number of events is indicated. (**D**) Complete workflow showing population identification steps and the sample comparison pipeline; details in *Materials and Methods*.

no. 6 bead subset reached a final frequency of 0.12% (Fig. 1C), which can be considered as rare (23).

We set up an AP workflow for the unbiased and automated study of population changes among different samples using established algorithms, as schematized in Fig. 1D and detailed in the *Materials and Methods*. An efficient subsampling procedure was needed to overcome the limitations of processing a large number of events while preserving rare cell subset representation. Because it performed better than random subsampling, the local density-dependent method (14) is applied to each individual sample (Supplemental Fig. 1a, 1b). For data visualization, we apply t-SNE (15), a nonlinear dimensionality reduction algorithm that was previously used to graphically represent cytometry data (19, 21). To identify cell subpopulations, we tested four state-of-the-art unsupervised clustering methods: Phenograph (17), DenseVM (18), ClusterX (19), and flowMeans (20) (Supplemental Fig. 1c). Phenograph outperformed the other methods and was therefore implemented in the AP workflow for data clustering. The workflow next recovers original events (upsampling) as output fcs files. These include the assigned cluster annotation (Cluster no.) and t-SNE coordinates that can be used to represent dot plots using conventional cytometry analysis software. Additional data analysis outputs obtained with the AP workflow include 1) t-SNE representations color coded according to the expression intensity of the various markers or according to the Phenograph-assigned cluster annotations, 2) cluster-based heatmap representations of the fluorescence

Downloaded from http://www.jimmunol.org/ at Fundacion (CNIC) on November 16, 2022

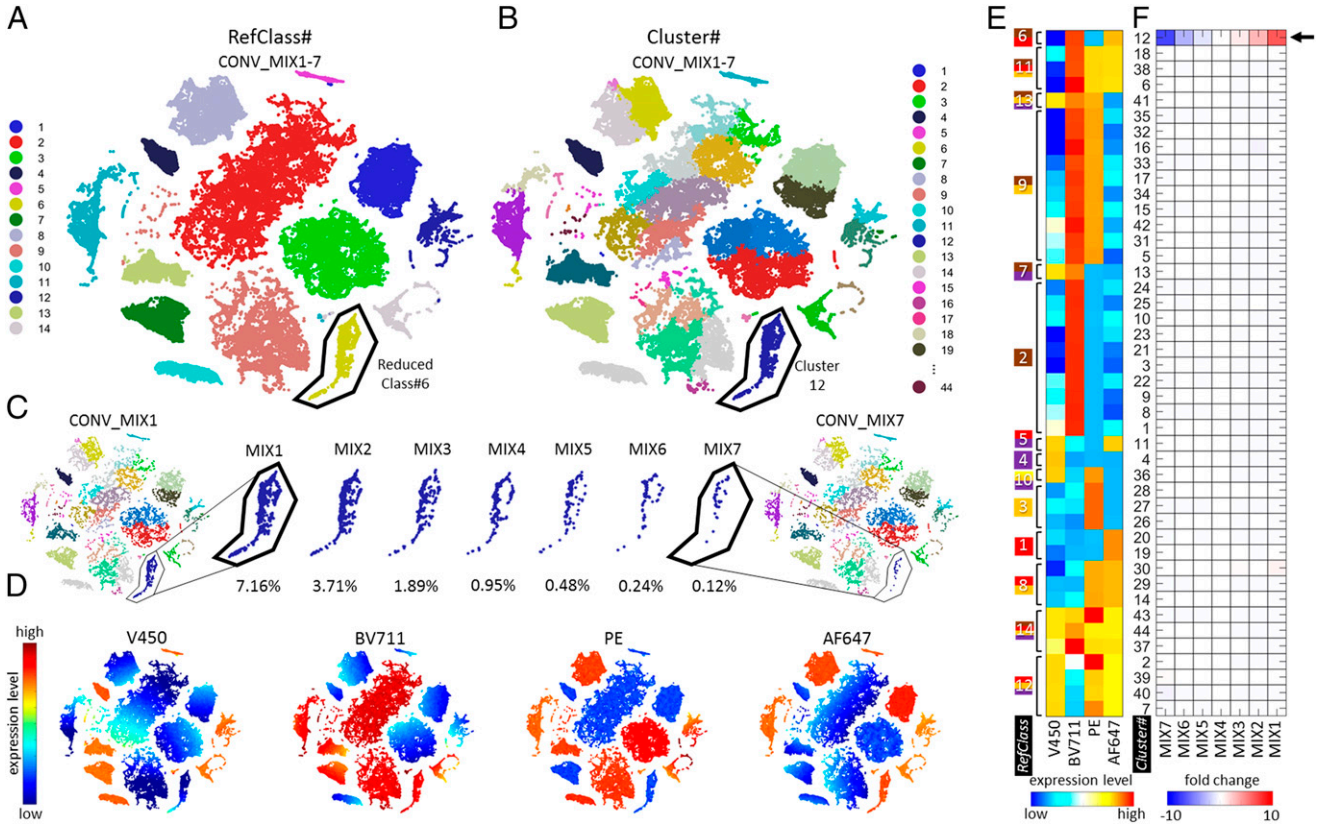

FIGURE 2. Automated analysis of the reference standard experiment by conventional cytometry. The reference standard experiment was acquired in a conventional flow cytometer in standard mode. (**A** and **B**) t-SNE projections of all synthetic samples (CONV_MIX1-7) color coded according to fluorochrome staining (RefClass no.) (A) and Phenograph cluster annotation (Cluster no.) (B). (**C**) t-SNE representation of individual samples (CONV_MIX1 to 7), highlighting events belonging to RefClass no. 6 and indicating the percentage of the total number of events in each synthetic file. (**D**) t-SNE map of all synthetic samples CONV_MIX1-7 color coded according to the expression level of the indicated fluorochrome. (**E**) Heatmap color coded according to mean fluorochrome expression (bottom) in each resulting cluster (main panel). Clusters were ordered by hierarchical clustering, grouping them in accordance with the actual staining (RefClass no.) as indicated (to the left of the main panel). (**F**) Heatmap color coded according to the fold differences in clusters (listed on the left) of samples (bottom) with respect to the MIX4 sample.

intensity acquired in the different detection channels of the flow cytometer, and 3) heatmaps showing fold differences in the frequency of each cluster in samples of interest, relative to some reference sample or group of samples. These representations allow comparison of different biological specimens, a key component of most questions addressed by FCM.

Synthetic CONV_MIX samples acquired in a conventional cytometer were used as ground-truth data to validate the analysis framework. All the files (CONV_MIX1-7) were displayed together in a t-SNE map, which was color coded either according to the reference class annotation (RefClass no.) as identified through manual gating (Fig. 2A) or to the cluster ID (Cluster no.) obtained by Phenograph (Fig. 2B). Cluster no. 12, corresponding to the serially reduced RefClass no. 6 subset, was automatically detected as an independent subset in all samples, including MIX7, in which this subset represents 0.12% of the total number of events analyzed (Fig. 2C). This result thus demonstrates the high sensitivity of the workflow for detecting rare subsets. The expression intensity of the different fluorochromes used for bead staining was represented as a color code in the t-SNE display (Fig. 2D). A heatmap was generated to display the fluorescence fingerprinting of each detected cluster (Fig. 2E), confirming the identity of Cluster no. 12 as the bead subset stained with AF647/BV711 (RefClass no. 6). Heatmap representation of fold differences in the frequency of Phenograph-annotated clusters showed that the AP workflow is able to automatically detect changes in Cluster no. 12 in distinct synthetic samples (Fig. 2F), further validating the ability of the workflow to automatically detect changes in subpopulations within samples.

Evaluation of AP across different data input modes

It is currently unknown how AP is affected by the instrument configuration used for data collection or the spillover correction modes used for data preprocessing (hereafter data input modes). To explore this, reference test tubes were acquired in both a conventional and a spectral flow cytometer in parallel, thus producing two synthetic reference datasets, called CONV and SPC. For the conventionally acquired dataset (CONV_MIX1-7), three data inputs were analyzed (Fig. 3A). They correspond to the compensated (CONV_4ch_CC) and uncompensated (CONV_4ch_NC) signals obtained from four fluorescence channels using a standard acquisition setup (i.e., the instrument detector configuration that best matched the panel of fluorochromes used for labeling) and an additional data input including the uncompensated signal from all fluorescence detectors available in the instrument. These include 16 fluorescence channels (CONV_16ch_NC) and can

Downloaded from http://www.jimmunol.org/ at Fundacion (CNIC) on November 16, 2022

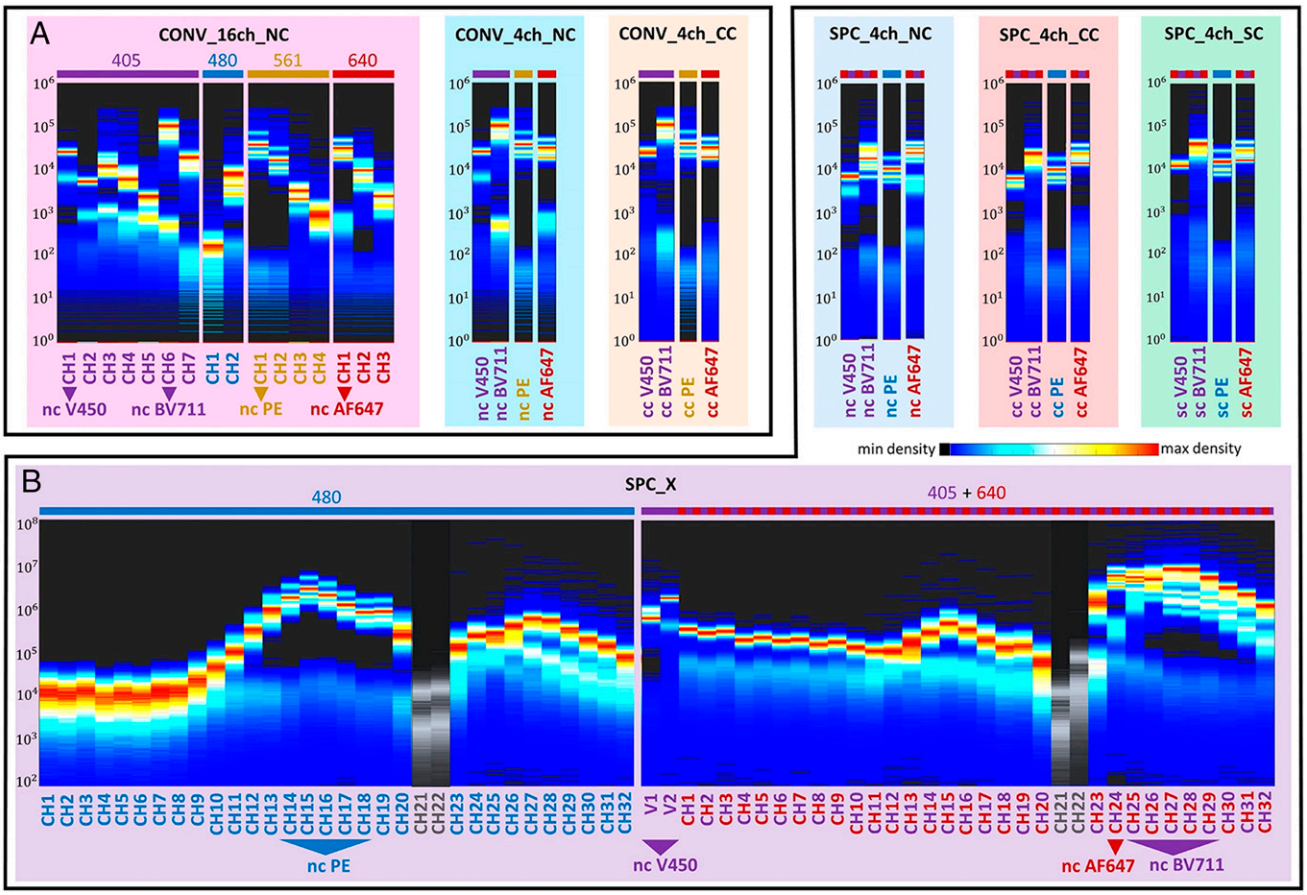

FIGURE 3. Data input modes based on cytometer detector configuration and data preprocessing. The reference standard experiment was acquired using either a conventional flow cytometer (**A**) or a spectral flow cytometer (**B**). Color-coded histograms represent densities of specific fluorescence intensities (log scale) for each detection channel (combination of excitation laser and detector). Channels are ordered first by the wavelengths of the independent excitation lasers (405, 480, 561, 640 nm) (top) and second by the wavelengths of their corresponding detectors (CH1, CH2, etc.) (bottom). (**A**) Input modes from a conventional flow cytometer acquisition. The pseudospectrum (CONV_16ch_NC) includes the fluorescence signals from 16 detectors. The correspondence of the pseudospectral channels to the four standard uncompensated channels is indicated at the bottom of the histogram. The uncompensated signals (CONV_4ch_NC) and compensated signals (CONV_4ch_CC) were obtained with a standard acquisition setup. (**B**) Input modes from the spectral cytometer acquisition. The panels show the full raw spectral data with 66 channels (SPC_X). The processed versions of spectra integrated into four channels include uncompensated signals (SPC_4ch_NC), conventionally compensated signals (SPC_4ch_CC), and signals compensated by spectral unmixing (SPC_4ch_SC). The correspondence of spectral channels to the four uncompensated channels is indicated at the bottom of the SPC_X histogram. CH21 and CH22 detectors are depicted in gray because they are blocked when the 640 nm laser is active. Density colors are normalized for each individual channel.

thus be considered a pseudospectrum because it contains the most complete spectral information available in this particular instrument optical configuration. Four of these channels are included in the CONV_4ch_NC data input, and the other 12 would in principle not be collected with a standard instrument acquisition setup because the wavelengths are not suited to the fluorochromes in the panel. The spectral dataset SPC_MIX1-7 was acquired in parallel in a system capable of continuous spectra data collection between 400 and 800 nm. SPC_MIX1-7 were processed to produce four data inputs (Fig. 3B). SPC_X corresponds to the complete fluorescence spectral raw data; the three other data inputs were configured to be equivalent to conventional cytometry data by integrating the signal from the 32 fluorescence detectors into four synthetic channels matching the specific fluorochromes used, as is common practice for manual analysis. These four channel data inputs were either left uncompensated (SPC_4ch_NC) or were automatically compensated using either conventional procedures (SPC_4ch_CC) or an unmixing algorithm for spectral compensation (SPC_4ch_SC).

The various data inputs were subjected to independent phenotypic analysis in the AP workflow. The detection accuracy for all reference bead subsets (RefClass no. 1 to 14) was evaluated using F1 measurement as previously reported (24, 25), scoring the correspondence between reference classes and automated clustering outputs as described by Weber and Robinson (16) (see *Materials and Methods*). Fig 4A shows plots of the final F1 scores for all events and reference classes in 10 independent runs of the AP workflow for each data input. Surprisingly, for conventional FCM data, raw pseudospectral data from uncompensated 16 fluorescence channel acquisition (CONV_16ch_NC) significantly outperformed both conventional compensated and uncompensated standard four channel data (CONV_4ch_CC and _NC). This result suggests that the 12 additional detection channels used in this dataset, although not suited to the fluorescence emission from the fluorochromes used, may carry valuable spectral information that improves the performance of automated analysis. Both the compensated CONV_4ch_CC and the uncompensated CONV_4ch_NC data inputs yielded similar phenotyping

Downloaded from http://www.jimmunol.org/ at Fundacion (CNIC) on November 16, 2022

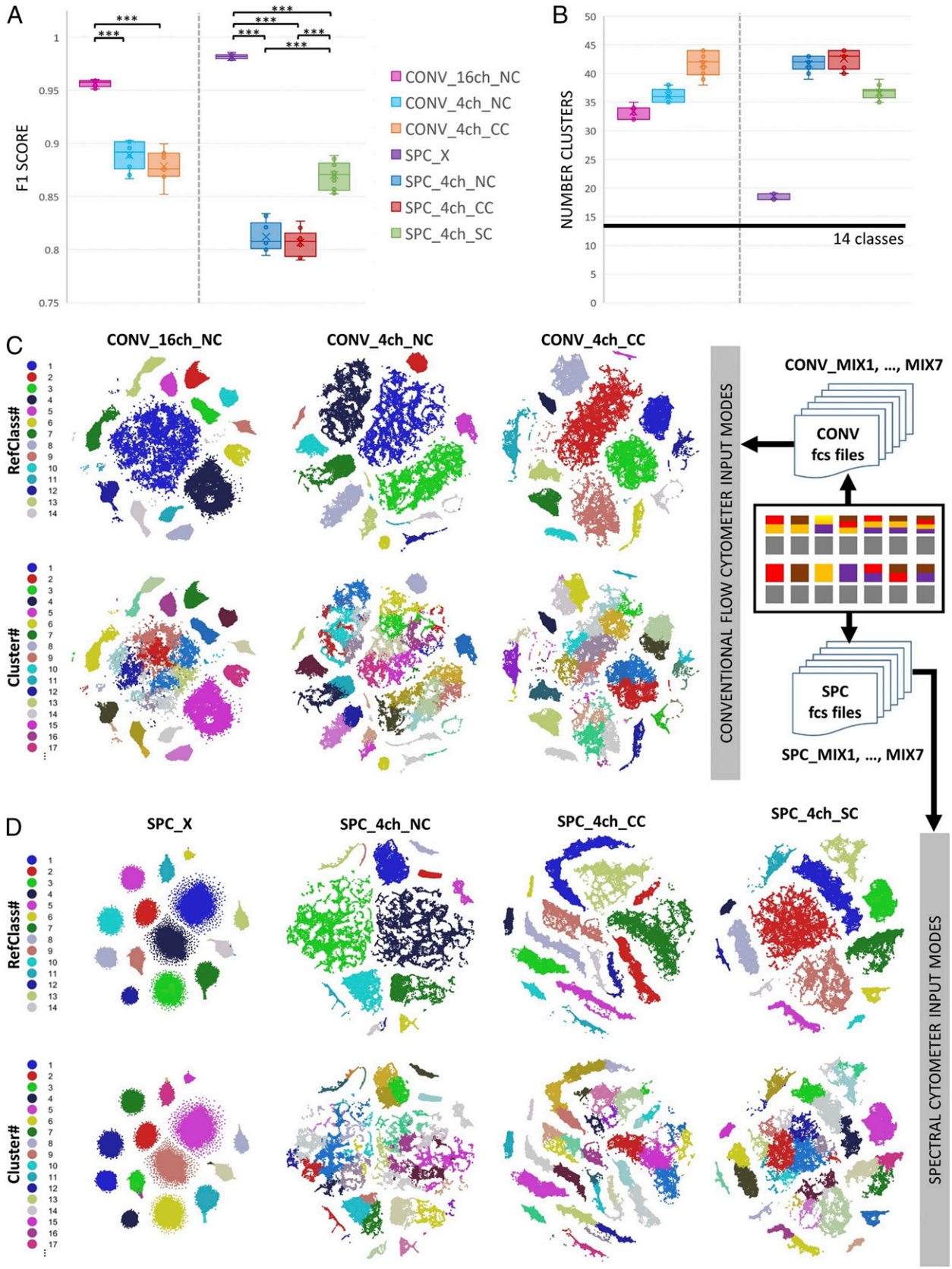

FIGURE 4. Evaluation of clustering performance in reference standard dataset across data input modes. The reference standard experiment was acquired in a conventional or spectral flow cytometer, and a dataset was produced including all the different conventional and spectral input modes. The boxplots show (**A**) F1 scores measuring the ability of Phenograph to recover the reference classes of events from all MIX1-7 samples (***$p < 0.001$) and (**B**) the number of clusters detected by Phenograph clustering for the different data inputs. For reference, the threshold lines are drawn for the expected 14 reference classes. (**C** and **D**) t-SNE maps of all synthetic samples color coded by reference class (RefClass no., first row) and output cluster number (Cluster no., second row) for conventional (C) and spectral (D) cytometer input modes.

Downloaded from http://www.jimmunol.org/ at Fundacion (CNIC) on November 16, 2022

performances, suggesting that data compensation is dispensable for automated analysis. In accordance with these results, the performance of the AP pipeline with the four data inputs obtained by spectral cytometry revealed a notable advantage of the raw spectrum (SPC_X) over any other data processing mode (Fig. 4A). Results were more accurate when using data preprocessed by spectral unmixing compensation (SPC_4ch_SC) as compared with data from the other two preprocessed-data inputs (SPC_4ch_CC and SPC_4ch_NC). These two inputs showed no significant difference in performance, confirming that compensation using conventional procedures offers no advantages for AP. Overall, raw spectral data (SPC_X) produced higher accuracy than any other data mode in either conventional or spectral cytometry. Compared with other data inputs, raw spectra (SPC_X) yielded a number of detected clusters that better matched the number of reference classes available (14 populations). All conventional and spectral FCM data inputs resulted in overestimates of the number of clusters (Fig. 4B). Different unsupervised clustering algorithms generated similar results from the same dataset (Supplemental Fig. 2), again evidencing the advantages of full-spectral and pseudospectral input modes. Both full-spectral (SPC_X) and pseudospectral (CONV_16ch_NC) input modes originate t-SNE maps with a highly condensed spatial representation of reference classes. Thus, these input modes yielded a better definition of populations, a higher overlap between Phenograh clusters (Cluster no.) and reference classes (RefClass no.), and less overclustering than other input modes (Fig. 4C, 4D). Interestingly, these maps also show how compensation can produce higher spatial data dispersion (related to the persistent gradient-like distribution of fluorescence signals); this is due to spillover spreading effects as evidenced in modes CONV_4ch_CC and SPC_4ch_CC. An example of this effect can be observed for RefClass no. 2 (red), corresponding to the single-stained BV711 population (Fig. 4C, 4D). These results demonstrate that acquiring more information in a flow cytometer, regardless of whether the detection channels match the fluorochrome emissions, improves the clustering results and thus increases the accuracy of AP. Our data further reveal that compensation procedures do not improve phenotyping results. In the light of these results, a set of guidelines for FCM data preparation for automated analysis can be drawn that substantially differ from the standard procedures used for manual gate-based analysis (Table I).

Advantages of raw spectral or pseudospectral data input modes for the automated detection of changes in dendritic cell subsets from Batf3-deficient mice

Basic leucine zipper transcription factor, ATF-like 3 (Batf3), is essential for the development of the CD103$^+$ subset of dendritic cells (DCs) (11, 26–28). Skin-draining LNs from Batf3$^{-/-}$ mice in the C57BL/6 background show significant reduction in the CD11c$^+$/CD40$^+$/MHC II$^+$/CD103$^+$ migratory DCs. This population is rare in WT mice (0.1%) and is reduced to 0.03% in Batf3$^{-/-}$ mice (12). To test the AP workflow against data input modes in real complex samples, we used it for unbiased phenotyping and automated detection of cell population differences between LN samples from WT and Batf$^{-/-}$ mice. We assessed the detection of

Table I. FCM acquisition, configuration, and data preprocessing guidelines for common tasks of manual and automated analyses

		Cytometry Technology in Use			
		Conventional		Spectral	
	Recommended for	Data Input Mode Recommended	Guidelines	Data Input Mode Recommended	Guidelines
Automated	Unbiased population detection	PX: pseudospectral	Use all detectors available No spillover correction and/or compensation	X: full spectral	Use all physical detectors available No spillover correction and/or compensation
Manual	Knowledge-based population detection and interpretation and/or identification	CC: conventionally compensated	Use detectors matching fluorochromes in panel Conventional compensation	SC: spectrally compensated	Use virtual detectors (integrated virtual channels) matching fluorochromes in panel Spectral unmixing
Based on multidimensional representation of data					
Based on serial 2D representations and gating of data					

2D, two-dimensional.

Downloaded from http://www.jimmunol.org/ at Fundacion (CNIC) on November 16, 2022

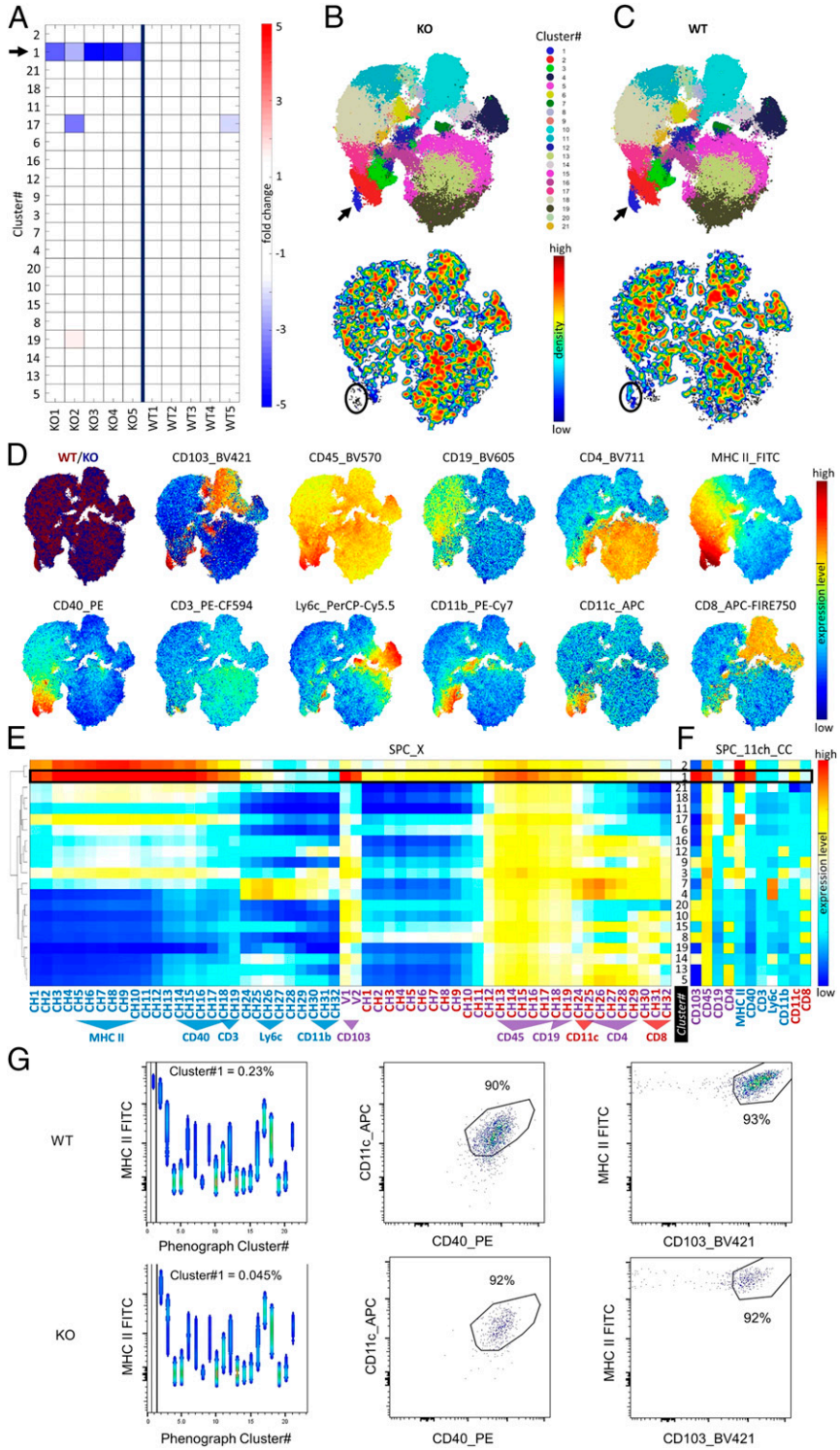

FIGURE 5. Automated analysis of differences in skin-draining LN cell populations from Baft-deficient mice using raw spectral data as input. Skin-draining LN cells from WT and Batf3$^{-/-}$ mice were stained and acquired using spectral FCM to produce raw spectral data (SPC_X). (**A**) Heatmap displaying the fold differences in frequencies in automatically detected clusters for the indicated samples (bottom) with respect to the mean values for WT mice. Arrow highlights one cluster showing clear differences between WT and Batf3$^{-/-}$ mice. Cluster numbers are ordered accordingly to hierarchical clustering output using the raw spectral signal, as displayed in (**E**). (**B** and **C**) t-SNE map displaying Phenograph cluster number (top row) and cell density (bottom row) in LN cells from KO mice [Batf3$^{-/-}$; (B)] and WT mice (C). Arrows and circles mark the location of Cluster no. 1, which shows a lower density in KO mice. (**D**) t-SNE maps color coded by the expression of different conventionally compensated markers as indicated. (E and **F**) Heatmaps displaying the fluorescence fingerprinting for each cluster (raw spectral mode, SPC_X) (E) and the corresponding traditional input mode with conventional compensation (SPC_11ch_CC) (F). (**G**) Manual gating analysis using conventional FCM software allows the identification of Cluster no. 1 as CD11c^{+}/MHC II^{+}/CD40^{+}/CD103^{+} migratory DCs. The percentages of the gated subsets (circled sections) are shown relative to the total number of events.

CD103^{+} DCs among mouse LN cells labeled with a panel of 11 Abs with signals acquired by conventional and spectral FCM. Results from spectral FCM obtained with the raw spectral data input mode (SPC_X) are presented in Fig. 5. The heatmap represents the fold difference in the cluster frequency obtained from unsupervised Phenograph clustering of LNs from five Batf3$^{-/-}$ mice relative to the mean value from the LN samples from five WT mice (Fig. 5A). This analysis highlighted Cluster no. 1, which was reduced in all the Batf3$^{-/-}$ mice ($p < 0.001$), with a mean 4.175-fold decrease (Fig. 5A). Representative t-SNE maps color coded according to cluster annotation and density reveal a reduction in Batf3$^{-/-}$ samples of a clearly differentiated group of cells corresponding to Cluster no. 1 (Fig. 5B, 5C). t-SNE representations were also color coded according to the expression intensity of the 11 conventionally compensated fluorochromes used for staining (Fig. 5D). Heatmaps represent the intensities of raw spectral channels (SPC_X) (Fig. 5E) and the

Downloaded from http://www.jimmunol.org/ at Fundacion (CNIC) on November 16, 2022

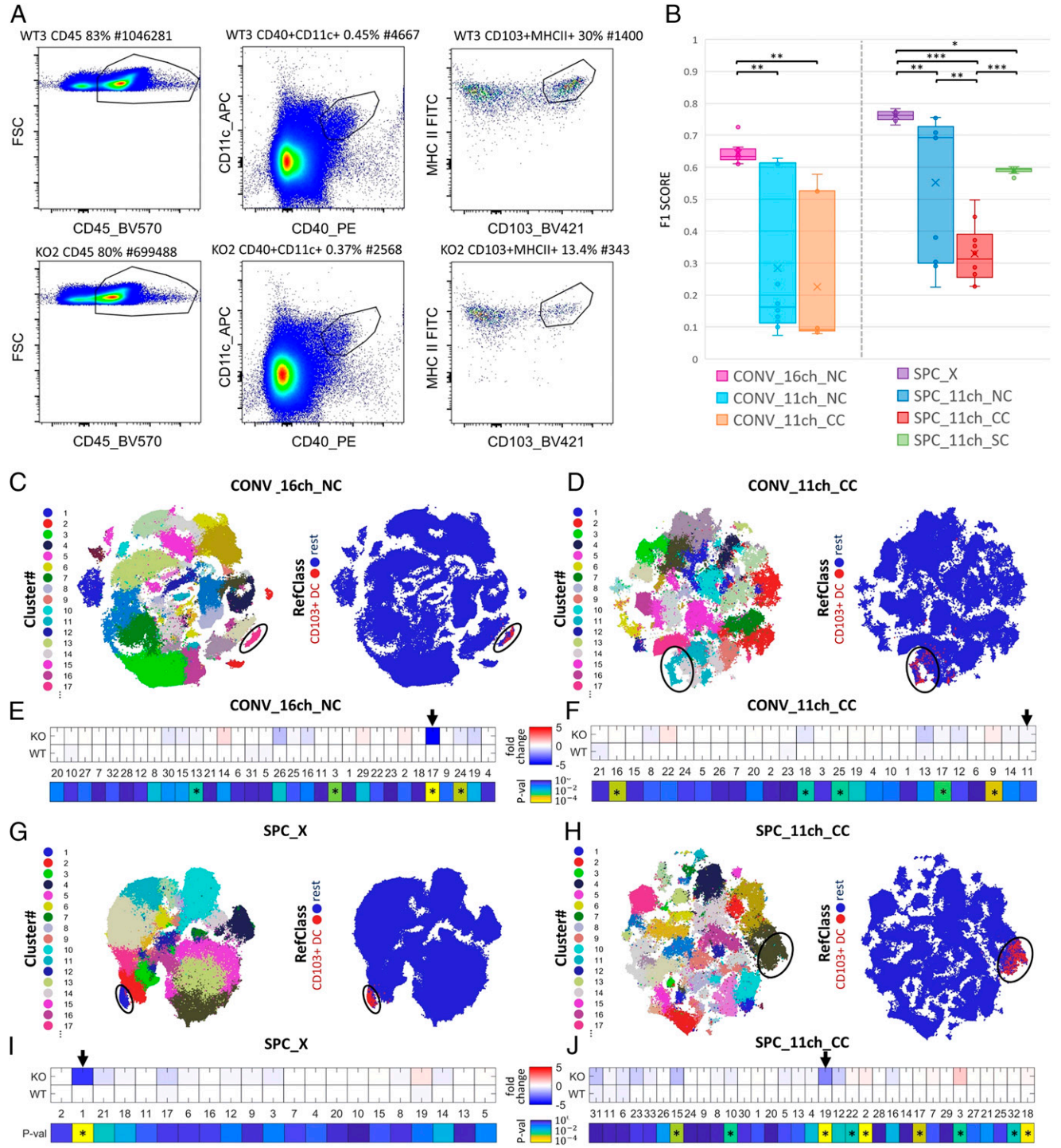

FIGURE 6. Evaluation of data input modes in the automated detection of changes in CD103$^+$ DCs in Batf3-deficient mice. Skin-draining LN cells from WT and Batf3$^{-/-}$ mice were stained and acquired with conventional and spectral flow cytometers, and data input modes were prepared as indicated in *Materials and Methods*. (**A**) Manual gating for labeling the target CD103$^+$ DC population based on expression of CD45, CD11c, CD40, MHC II, and CD103, as indicated. The percentages of the gated subsets (circled sections) are shown relative to the number of events gated in previous steps. (**B**) F1 scores measuring the detection accuracy for CD103$^+$ DCs as an independent population in all WT and Batf3$^{-/-}$ samples (*$p < 0.05$, **$p < 0.01$, ***$p < 0.001$). (**C**, **D**, **G**, and **H**) t-SNE maps color coded by Cluster no. and RefClass for the CONV_16ch_NC (C), CONV_11h_CC (D), SPC_X (G), and SPC_11ch_CC (H) data input modes. The CD103$^+$ DC target population is highlighted with circles. (**E**, **F**, **I**, and **J**) Heatmaps of mean fold difference in the frequencies of each detected cluster between WT and KO mice (top) and of p values obtained upon comparison of raw frequencies between the two genotypes (bottom) for the different input modes, as indicated. Black arrows mark the Cluster no. that best fits the CD103$^+$ DC population. *$p < 0.01$.

corresponding traditional input mode with signals integrated into 11 channels after conventional compensation (SPC_11ch_CC) (Fig. 5F). These representations allow visual inspection of marker expression in the Cluster no. 1 subset. Output fcs files containing the cluster annotation as a new parameter were subsequently analyzed by manual gating-based FCM analysis (Fig. 5G). Cluster no. 1 annotated cells were gated and represented as biaxial dot plots, identifying

Downloaded from http://www.jimmunol.org/ at Fundacion (CNIC) on November 16, 2022

cells detected in this cluster as CD11c$^+$/MHC II$^+$/CD40$^+$/CD103$^+$ migratory DCs, in line with previous reports (12). The precision of the clustering seemed high, with the CD103$^+$ DC subpopulation representing 93 and 92% of the total number of Cluster no. 1–annotated cells for WT and Batf3$^{-/-}$ samples, respectively. These results further confirm the ability of the AP framework to detect differences between real DC subpopulations when using raw spectral data as the input. Similar results were obtained using conventional cytometry with the pseudospectral CONV_16ch_NC data input mode (Supplemental Fig. 3).

To evaluate how data input modes affect the performance of the AP workflow in the detection of real DC subpopulations, we prepared a reference standard by manually gating the CD103$^+$ DC subpopulation according to the expression of CD45, CD11c, CD40 and MHC II, and CD103 (Fig. 6A). Mean F1 scores measured the detection accuracy for the manually gated reference CD103$^+$ DC subpopulation in 10 independent analysis runs for each data input mode. In conventional cytometry, the only data input that consistently enabled the efficient detection of this subpopulation was the pseudospectrum (CONV_16ch_NC; mean F1 score 0.64) (Fig 6B). For spectral cytometry data, the highest detection accuracy for CD103$^+$ DCs was obtained with the raw spectra (SPC_X) data mode (Fig 6B), which gave F1 scores above 0.73. Spectral compensation input mode (SPC_11ch_SC) performed more accurately and consistently than the SPC_11ch_CC and SPC_11ch_NC modes, which yielded lower accuracies and more variable results. Thus, the full-spectral or pseudospectral modes allowed the most efficient detection of the target population, superior to the standard setup data inputs. This finding is supported by t-SNE maps for the pseudospectral (Fig. 6C) and spectral modes (Fig. 6G), which reveal a higher spatial condensation of the target CD103$^+$ DC population to confined areas, with a lower contribution of cells from different clusters than obtained with conventional compensated data inputs (Fig. 6D, 6H) or noncompensated data inputs (Supplemental Fig. 4). The CD103$^+$ DC subpopulation is reduced in the LNs of Batf3$^{-/-}$ mice (12) (Fig. 5), and this allowed us to evaluate the influence of the different data modes on the ability of the AP workflow to detect significant between-sample differences. In accordance with their ability to consistently detect the target DC subpopulation, the spectral and pseudospectral input modes enabled detection of statistically significant fold differences between WT and Batf3$^{-/-}$ mice (Fig. 6E, 6I). The lower accuracy of the conventional compensated data input modes in detecting the target migratory DCs as a specific cell subset resulted in less statistically significant fold difference scores for this population (Fig. 6F, 6J). Moreover, the spectral and pseudospectral input modes reduced the false-positive detection of changes in clusters that either did not represent real cell subpopulations or were found in individual KO mice but not consistently in all of them (Fig. 6E, 6I). Other standard data inputs either revealed no significant differences in the target population or detected more false positives (Fig. 6F, 6J, Supplemental Fig. 4). These results further demonstrate the importance of data preparation, confirming the advantages of raw spectral or pseudospectral data for the consistent detection of changes in rare subpopulations in real LN samples.

Discussion

We produced annotated FCM datasets from samples acquired using conventional or spectral FCM technologies in an unprecedented effort, to our knowledge, to evaluate how different data acquisition configurations and preprocessing modes affect the automated phenotypic analysis of cell populations. For automated analysis, we implemented a workflow that uses unsupervised state-of-the-art algorithms of data sampling, visualization, and clustering, enabling the computationally efficient automated detection of frequency changes among phenotypically distinct populations in multiple samples. The number of publicly available algorithms for computer-aided phenotyping is growing continuously (14, 17, 19–21, 29–35). We did not attempt to test the performance of these algorithms because this has been addressed in other studies (16, 24, 36). These studies have revealed a variability in performance that is highly dependent on the dataset used, which is related in part to the data dimensionality. Because we sought an unbiased phenotyping method, we focused on automated algorithms that make no prior assumptions about cluster size or number of expected populations. We followed the recommendations of Weber and Robinson (16) and tested the high-performance algorithms Phenograph (17) and flowMeans (20), which are based on nearest-neighbor and *k*-means, respectively. The other recommended algorithm (X-shift) was not tested because it cannot be run in script mode. Another two algorithms, ClusterX (19) and DenseVM (18), were tested because they rely on t-SNE projections. The best performance was obtained with Phenograph, which was therefore implemented in the AP workflow.

Public initiatives have addressed the performance of computational analysis methods (FlowCAP) (24, 36). To the best of our knowledge, these initiatives have not considered data inputs diferent than the standard ones for subsequent analysis. Earlier reports evaluating high-dimensional data analysis techniques relied on both mass cytometry and FCM datasets, with the FCM datasets acquired using standard cytometry data collection setups (16, 32, 37). Our results demonstrate that the quality of results generated with automated analysis workflows is strongly influenced by the configuration of cytometer acquisition detectors and the data preprocessing steps. Therefore, a careful choice of data input is critical for obtaining best performance of AP. The most accurate phenotyping was obtained with raw data acquired in a spectral cytometer; however, similar performance was obtained with the pseudospectral raw data input, which was obtained using the full detector resources of our conventional cytometer (16 detectors instead of the standard <16-detector setup). Importantly, all the clustering algorithms tested performed similarly, evidencing the advantages of spectral or pseudospectral raw data inputs over conventional optical configurations. The analysis of data obtained with a conventional cytometer highlights the futility of applying data compensation preprocessing steps, as this did not improve AP performance. This finding is consistent with the aim of data compensation being to visualize data in two dimensions to aid human interpretation, an irrelevance when analysis is unsupervised and carried out in a multidimensional computational environment. In agreement with this, when data were acquired using spectral cytometry technology, the spectrally compensated data mode was significantly less efficient than

Downloaded from http://www.jimmunol.org/ at Fundacion (CNIC) on November 16, 2022

the raw spectral data mode at enabling automated detection of cell populations. The efficiency of automated clustering was further reduced by integration of spectral data into channels matching fluorochromes, regardless of whether the data were compensated or uncompensated. These data input modes involve a loss of information when the full spectrum is integrated into discrete channels, again suggesting that "the more information the better" when acquiring FCM data for AP. Our results may be explained by the fact that compensation and data integration neglect factors such as the signal from donor fluorochromes in tandem dyes and cell-fluorochrome interactions, leading to changes in the fluorescence emission spectrum; these factors can help to differentiate cell subsets and therefore can be useful for their efficient automated detection. Accordingly, uncompensated data were used as input in the development of the *immuno*Clust algorithm (33); although, to our knowledge, neither this nor other studies provided a formal evaluation of different data inputs. We believe that the datasets presented in this paper using different data input modes are of high interest for the future development and evaluation of new analysis algorithms and made them available (see *Materials and Methods*).

For data preparation for automated phenotypic analysis, most reports recommend FCM dataset acquisition with the standard instrument optical configuration and compensation (10, 24, 32, 37). Our study represents a departure from established procedures for FCM data preparation by demonstrating the advantages of raw data over compensated data. Moreover, our results advise against using the standard FCM optical configuration, limited to the detection channels matching the fluorescence emission of the fluorophores in use. Instead, we recommend that the instrument be configured to use all available fluorescence detectors for data acquisition, ideally covering the complete fluorescence spectrum to improve automated phenotypic analysis. Our study is, therefore, especially relevant in an era in which FCM technology is moving toward an increasing number of fluorescence detectors available for simultaneous parameter acquisition. These guidelines should be taken into account in the future acquisition of FCM data by immunology research efforts and by public initiatives evaluating computational analysis tools, such as FlowCAP, or consortia dealing with FCM data for population studies, such as the Human Immunology Project Consortium. These recommendations could also be useful for automated analysis of spectral or pseudospectral data previously acquired and stored by these initiatives, opening the door to new discoveries. Our recommendations promote a more effective use of the technology available in each laboratory and will contribute to the widespread use of automated analysis techniques within the FCM community.

Acknowledgments

We thank Irene Palacios, Elena Prieto, Mariano Vitón, and Raquel Nieto for excellent technical assistance and Dr. Salvador Iborra for helpful discussion of dendritic cell studies. Editorial assistance was provided by Simon Bartlett.

Disclosures

The authors have no financial conflicts of interest.

References

1. Spitzer, M. H., and G. P. Nolan. 2016. Mass cytometry: single cells, many features. *Cell* 165: 780–791.
2. Saeys, Y., S. Van Gassen, and B. N. Lambrecht. 2016. Computational flow cytometry: helping to make sense of high-dimensional immunology data. *Nat. Rev. Immunol.* 16: 449–462.
3. Roederer, M. 2001. Spectral compensation for flow cytometry: visualization artifacts, limitations, and caveats. *Cytometry* 45: 194–205.
4. Kalina, T., J. Flores-Montero, V. H. J. van der Velden, M. Martin-Ayuso, S. Böttcher, M. Ritgen, J. Almeida, L. Lhermitte, V. Asnafi, A. Mendonça, et al; EuroFlow Consortium (EU-FP6, LSHB-CT-2006-018708). 2012. EuroFlow standardization of flow cytometer instrument settings and immunophenotyping protocols. *Leukemia* 26: 1986–2010.
5. Herzenberg, L. A., J. Tung, W. A. Moore, L. A. Herzenberg, and D. R. Parks. 2006. Interpreting flow cytometry data: a guide for the perplexed. *Nat. Immunol.* 7: 681–685.
6. Grégori, G., V. Patsekin, B. Rajwa, J. Jones, K. Ragheb, C. Holdman, and J. P. Robinson. 2012. Hyperspectral cytometry at the single-cell level using a 32-channel photodetector. *Cytom. Part A* 81: 35–44.
7. Schmutz, S., M. Valente, A. Cumano, and S. Novault. 2016. Spectral cytometry has unique properties allowing multicolor analysis of cell suspensions isolated from solid tissues. *PLoS One* 11: e0159961.
8. Nolan, J. P., and D. Condello. 2001. Spectral flow cytometry. In *Current Protocols in Cytometry*. John Wiley & Sons, Inc., Hoboken, NJ, p. 1.27.1–1.27-13.
9. Chester, C., and H. T. Maecker. 2015. Algorithmic tools for mining high-dimensional cytometry data. *J. Immunol.* 195: 773–779.
10. Mair, F., F. J. Hartmann, D. Mrdjen, V. Tosevski, C. Krieg, and B. Becher. 2016. The end of gating? An introduction to automated analysis of high dimensional cytometry data. *Eur. J. Immunol.* 46: 34–43.
11. Hildner, K., B. T. Edelson, W. E. Purtha, M. Diamond, H. Matsushita, M. Kohyama, B. Calderon, B. U. Schraml, E. R. Unanue, M. S. Diamond, et al. 2008. Batf3 deficiency reveals a critical role for CD8alpha+ dendritic cells in cytotoxic T cell immunity. *Science* 322: 1097–1100.
12. Martínez-López, M., S. Iborra, R. Conde-Garrosa, and D. Sancho. 2015. Batf3-dependent CD103+ dendritic cells are major producers of IL-12 that drive local Th1 immunity against *Leishmania major* infection in mice. *Eur. J. Immunol.* 45: 119–129.
13. Parks, D. R., M. Roederer, and W. A. Moore. 2006. A new "Logicle" display method avoids deceptive effects of logarithmic scaling for low signals and compensated data. *Cytometry A.* 69: 541–551.
14. Qiu, P., E. F. Simonds, S. C. Bendall, K. D. Gibbs, Jr., R. V. Bruggner, M. D. Linderman, K. Sachs, G. P. Nolan, and S. K. Plevritis. 2011. Extracting a cellular hierarchy from high-dimensional cytometry data with SPADE. *Nat. Biotechnol.* 29: 886–891.
15. Van Der Maaten, L. 2014. Accelerating t-SNE using tree-based algorithms. *J. Mach. Learn. Res.* 15: 1–21.
16. Weber, L. M., and M. D. Robinson. 2016. Comparison of clustering methods for high-dimensional single-cell flow and mass cytometry data. *Cytometry A* 89: 1084–1096.
17. Levine, J. H., E. F. Simonds, S. C. Bendall, K. L. Davis, A. D. Amir, M. D. Tadmor, O. Litvin, H. G. Fienberg, A. Jager, E. R. Zunder, et al. 2015. Data-driven phenotypic dissection of AML reveals progenitor-like cells that correlate with prognosis. *Cell* 162: 184–197.
18. Shekhar, K., P. Brodin, M. M. Davis, and A. K. Chakraborty. 2014. Automatic classification of cellular expression by nonlinear stochastic embedding (ACCENSE). *Proc. Natl. Acad. Sci. USA* 111: 202–207.
19. Chen, H., M. C. Lau, M. T. Wong, E. W. Newell, M. Poidinger, and J. Chen. 2016. Cytofkit: a bioconductor package for an integrated mass cytometry data analysis pipeline. *PLOS Comput. Biol.* 12: e1005112.
20. Aghaeepour, N., R. Nikolic, H. H. Hoos, and R. R. Brinkman. 2011. Rapid cell population identification in flow cytometry data. *Cytometry A* 79: 6–13.
21. Amir, A. D., K. L. Davis, M. D. Tadmor, E. F. Simonds, J. H. Levine, S. C. Bendall, D. K. Shenfeld, S. Krishnaswamy, G. P. Nolan, and D. Pe'er. 2013. viSNE enables visualization of high dimensional single-cell data and reveals phenotypic heterogeneity of leukemia. *Nat. Biotechnol.* 31: 545–552.
22. Jonker, R., and A. Volgenant. 1987. A shortest augmenting path algorithm for dense and sparse linear assignment problems. *Computing* 38: 325–340.
23. Perfetto, S. P., P. K. Chattopadhyay, and M. Roederer. 2004. Seventeen-colour flow cytometry: unravelling the immune system. *Nat. Rev. Immunol.* 4: 648–655.
24. Aghaeepour, N., G. Finak, The FlowCAP Consortium, The DREAM Consortium, H. Hoos, T. R. Mosmann, R. Brinkman, R. Gottardo, and R. H. Scheuermann. 2013. Critical assessment of automated flow cytometry data analysis techniques. [Published erratum appears in 2013 *Nat. Methods.* 10: 445.] *Nat. Methods* 10: 228–238.
25. Weber, L. M., K. N. Hayda, and K. S. Anseth. 2008. Cell-matrix interactions improve beta-cell survival and insulin secretion in three-dimensional culture. *Tissue Eng. Part A* 14: 1959–1968.
26. Edelson, B. T., T. R. Bradstreet, W. Kc, K. Hildner, J. W. Herzog, J. Sim, J. H. Russell, T. L. Murphy, E. R. Unanue, and K. M. Murphy. 2011. Batf3-dependent CD11b(low/-) peripheral dendritic cells are GM-CSF-independent and are not required for Th cell priming after subcutaneous immunization. *PLoS One* 6: e25660.
27. Seillet, C., J. T. Jackson, K. A. Markey, H. J. M. Brady, G. R. Hill, K. P. A. Macdonald, S. L. Nutt, and G. T. Belz. 2013. CD8α+ DCs can be induced in the absence of transcription factors Id2, Nfil3, and Batf3. *Blood* 121: 1574–1583.

Downloaded from http://www.jimmunol.org/ at Fundacion (CNIC) on November 16, 2022

28. Waithman, J., D. Zanker, K. Xiao, S. Oveissi, B. Wylie, R. Ng, L. Tögel, and W. Chen. 2013. Resident CD8(+) and migratory CD103(+) dendritic cells control CD8 T cell immunity during acute influenza infection. *PLoS One* 8: e66136.
29. Samusik, N., Z. Good, M. H. Spitzer, K. L. Davis, and G. P. Nolan. 2016. Automated mapping of phenotype space with single-cell data. *Nat. Methods* 13: 493–496.
30. Anchang, B., T. D. P. Hart, S. C. Bendall, P. Qiu, Z. Bjornson, M. Linderman, G. P. Nolan, and S. K. Plevritis. 2016. Visualization and cellular hierarchy inference of single-cell data using SPADE. *Nat. Protoc.* 11: 1264–1279.
31. Bendall, S. C., E. F. Simonds, P. Qiu, E. D. Amir, P. O. Krutzik, R. Finck, R. V. Bruggner, R. Melamed, A. Trejo, O. I. Ornatsky et al. 2011. Single-cell mass cytometry of differential immune and drug responses across a human hematopoietic continuum. *Science* 332: 687–696.
32. Mosmann, T. R., I. Naim, J. Rebhahn, S. Datta, J. S. Cavenaugh, J. M. Weaver, and G. Sharma. 2014. SWIFT-scalable clustering for automated identification of rare cell populations in large, high-dimensional flow cytometry datasets, part 2: biological evaluation. *Cytometry A* 85: 422–433.
33. Sörensen, T., S. Baumgart, P. Durek, A. Grützkau, and T. Häupl. 2015. immunoClust–An automated analysis pipeline for the identification of immunophenotypic signatures in high-dimensional cytometric datasets. *Cytometry A* 87: 603–615.
34. Malek, M., M. J. Taghiyar, L. Chong, G. Finak, R. Gottardo, and R. R. Brinkman. 2015. flowDensity: reproducing manual gating of flow cytometry data by automated density-based cell population identification. *Bioinformatics* 31: 606–607.
35. Finak, G., A. Bashashati, R. Brinkman, and R. Gottardo. 2009. Merging mixture components for cell population identification in flow cytometry. *Adv. Bioinforma.* 2009: 247646.
36. Aghaeepour, N., P. Chattopadhyay, M. Chikina, T. Dhaene, S. Van Gassen, M. Kursa, B. N. Lambrecht, M. Malek, G. J. McLachlan, Y. Qian, et al. 2016. A benchmark for evaluation of algorithms for identification of cellular correlates of clinical outcomes. *Cytometry A* 89: 16–21.
37. Rundberg Nilsson, A., D. Bryder, and C. J. H. Pronk. 2013. Frequency determination of rare populations by flow cytometry: a hematopoietic stem cell perspective. *Cytometry A* 83: 721–727.

Downloaded from http://www.jimmunol.org/ at Fundacion (CNIC) on November 16, 2022